T. Kiyono[1], H. M. Noda[1], T. Kumagai[2], H. Oshio[3], Y. Yoshida[1], T. Matsunaga[1], and K. Hikosaka[4]

[1]Earth System Division, National Institute for Environmental Studies, Tsukuba, Japan.

[2]Graduate School of Agricultural and Life Sciences, The University of Tokyo, Bunkyo-ku, Japan.

[3]School of Environment and Society, Tokyo Institute of Technology, Yokohama, Japan.

[4]Graduate School of Life Sciences, Tohoku University, Sendai, Japan.

Corresponding author: Tomoki Kiyono (tomoki.kiyono@nies.go.jp)

Key Points:

- Satellite-observed chlorophyll fluorescence showed a nonlinear wilting pattern in response to soil droughts on the Mongolian Plateau.
- We modified the SCOPE model and its ancillary radiative-transfer inversion algorithm to adequately evaluate dryland features.
- The modifications enabled assessing the physiological control of photosynthesis and retrieving the wilting point of the study area.
-

Abstract

Although water availability strongly controls gross primary production (GPP), the impact of soil moisture content (wilting point) is poorly quantified on regional and global scales. In this study, we used 10-year observations of solar-induced chlorophyll fluorescence (SIF) from the GOSAT satellite to estimate the wilting point of a semiarid grassland on the Mongolian Plateau. Radiative-transfer model inversion and soil-vegetation-atmosphere transfer simulation were jointly conducted to distinguish the drought impacts on physiology from changes in leaf-canopy optical properties. We modified an existing inversion algorithm and the widely used SCOPE model to adequately evaluate dryland features, e.g., sparse canopy and strong convection. The modified model with retrieved parameters and calibrated to GOSAT SIF predicts realistic GPP values. We found that (1) the SIF yield estimated from GOSAT shows a clear sigmoidal pattern in relation to drought, and the estimated wilting point matches ground-based observations within ~0.01 m^3 m^{-3} for the soil moisture content, (2) tuning the maximum carboxylation rate improves SIF prediction after considering changes in leaf-canopy optical properties, implying that GOSAT detected drought stress in leaf-level photosynthesis, and (3) the surface energy balance has significant impacts on the grassland's SIF; the modified model reproduces observed SIF radiance well (mean bias = 0.004 mW m^{-2} nm^{-1} sr^{-1} in summer), whereas the original model predicts substantially low values under weak horizontal wind (unstable) conditions. Some model-observation mismatches in

the SIF suggest that more research is needed for fluorescence parametrization (e.g., photoinhibition) and additional observation constraints.

Plain Language Summary

Solar-induced chlorophyll fluorescence, a weak radiation emitted as a byproduct of photosynthesis, can potentially assess physiological status, which is especially promising to evaluate poorly-quantified soil drought (wilting) impacts on the carbon cycle. However, the potential of satellite-observed fluorescence to improve the wilting prediction by vegetation models has not been sufficiently explored because of the confounding of plants' physiological stress and visible damages (i.e., leaf browning and defoliation). In this study, we distinguished physiological wilting from visible damages by estimating leaf pigment contents and total leaf amounts from satellite-observed reflectance with the aid of a radiative transfer model and a state-of-the-art vegetation model. We found that some model modifications were necessary to adequately evaluate dryland features, e.g., sparse vegetation cover and thermally induced atmospheric flow. The observed fluorescence showed a clear nonlinear response to the soil moisture content, which is characteristic of wilting. Model-based analysis suggested that the nonlinear response resulted from physiological stress, and the estimated wilting point quantitatively matched well with ground-based observations. Since our approach is based on biophysical theories and satellite data, our findings and methods should help to understand and predict the terrestrial water and carbon cycles in other regions.

1 Introduction

Drought is a critical hazard for human society and ecosystems. For example, the recent rapid warming and long-lasting drought over the Mongolian Plateau have reduced water resources (e.g., Brutsaert & Sugita, 2008), caused land degradation and frequent dust storms (Lee & Sohn, 2011), and enhanced the risk of livestock mortality by reducing pasture production (Nandintsetseg et al., 2018). Since gross primary production (GPP) is fundamental and changes in advance of other biological processes, monitoring and modeling of the impacts of drought on GPP have received great attention (e.g., Fisher et al., 2020; J. Huang et al., 2017; A. Verhoef and Egea, 2014).

Satellite remote sensing has played a pivotal role in quantifying the terrestrial carbon and water cycles. However, satellite-based diagnostic GPP products, most of which depend on the Moderate Resolution Imaging Spectroradiometer (MODIS), often fail to track dryland interannual dynamics (Biederman et al., 2017; Stocker et al., 2019). This error may result from insufficient parametrization of the wilting point, i.e., the soil-moisture content (SMC) effect, which is frequently neglected in diagnostic GPP products. Introducing the wilting effect to the diagnosis potentially reduces estimates of the GPP by 10–19% globally and increases the interannual variability by more than 100% across one-fourth of vegetated lands (Stocker et al., 2019). The nonlinear feature of the wilting point is also poorly constrained in prognostic models (Rogers et al., 2017), and

it is a major driver of carbon cycle uncertainty between the earth system models (ESMs) investigated in the CMIP5 model intercomparison project (Trugman et al., 2018).

Spaceborne observations of solar-induced chlorophyll fluorescence (SIF) have attracted attention since its first global measurements by the Greenhouse gases Observing Satellite (GOSAT) launched in 2009 (Frankenberg & Berry, 2018). SIF is a weak radiation emitted as a byproduct of photosynthesis, and satellites often observe SIF reductions associated with drought (Jonard et al., 2020). However, the mechanistic links to GPP are still unclear; some leaf-level studies have shown that SIF is insensitive to (or even increases with) short-term droughts (see reviews; Jonard et al., 2020; Magney et al., 2020). Since drought directly affects CO_2/H_2O exchange while SIF is rooted in radiative transfer and photochemistry, it is important to distinguish leaf-level processes linked to the former (e.g., stomatal closure, carboxylation-capacity reductions) and the latter (e.g., photoinhibition, chlorophyll reductions) from canopy-level processes such as defoliation. Physical leaf-canopy radiative-transfer model inversion (e.g., W. Verhoef et al., 2018; Weiss & Barret, 2016) and the SCOPE model (Soil-Canopy Observation of Photosynthesis and Energy fluxes, van der Tol et al., 2009; Yang et al., 2021) can serve as the bases for process-oriented studies, such as those for the forthcoming FLEX satellite (Mohammed et al., 2014). Mechanistic links are essential to go beyond mere correlation and utilize SIF with prognostic models.

In this study, we attempted to estimate the wilting point of a semiarid grassland from satellite SIF, combined with observed spectral reflectance and radiative-transfer inversion, to separate optical property changes (e.g., defoliation and chlorophyll reductions) from other factors. Furthermore, we demonstrated how satellite SIF signals constrain grassland GPP through soil-vegetation-atmosphere transfer (SVAT) simulation by modifying the widely used SCOPE model. We proposed simple but important modifications to both the inversion algorithm and the SCOPE model, which are necessary to utilize satellite SIF products with relatively large footprints (GOSAT here) and evaluate the energy, water, and carbon fluxes in grassland ecosystems.

2 Study Area and Climate

The study area is the eastern end of the Mongolian Plateau (46–52 °N; 110–122 °E; elevation 700–1,000 m), which has experienced rapid warming and drought since the late 1990s (Xu et al., 2015). Figure 1 illustrates the land cover map, according to the International Geosphere-Biosphere Programme (IGBP) (Friedl & Sulla-Menashe, 2019). Typical plant species are cool-season C3 grasses (Y. Yan et al., 2018).

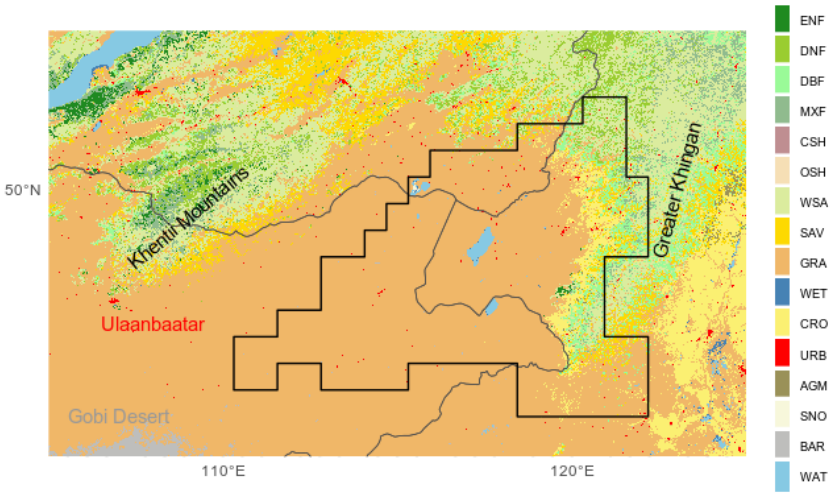

Figure 1. IGBP land cover map of the study area for 2015. Abbreviations represent evergreen needleleaf forests (ENF), deciduous needleleaf forests (DNF), deciduous broadleaf forests (DBF), mixed forests (MXF), closed shrublands (CSH), open shrublands (OSH), woody savannas (WSA), savannas (SAV), grasslands (GRA), wetlands (WET), croplands (CRO), urban areas (URB), agricultural mosaics (AGM), snow and ice (SNO), barren areas (BAR), and water bodies (WAT).

According to the Modern-Era Retrospective Analysis for Research and Applications, Version 2 (MERRA-2) reanalysis product (Gelaro et al., 2017), the annual precipitation is approximately 400 mm, and the maximum and minimum values of the 2-m air temperature are 35 °C and −35 °C, respectively. The study area boundaries were determined by hierarchical cluster analysis (Badr et al., 2015) using the monthly means of the MERRA-2 air temperature, precipitation, vapor pressure deficit, and the top-of-canopy (TOC) irradiance of photosynthetic active radiation (PAR) during 2009–2018. Since SMC products generally have large uncertainty (Li et al., 2021) and the MERRA-2 SMC is not assimilated with observational data, the reliability was confirmed by comparison with other datasets (Text S1 and Figure S1). We found that the MERRA-2 SMC is better than or as good as the other products.

3 Strategies of Inverse and Forward Simulations

Figure 2 overviews the model calibration procedure. Radiative-transfer model inversion and SVAT simulation were jointly conducted to distinguish the drought impacts on physiology from changes in leaf-canopy optical properties.

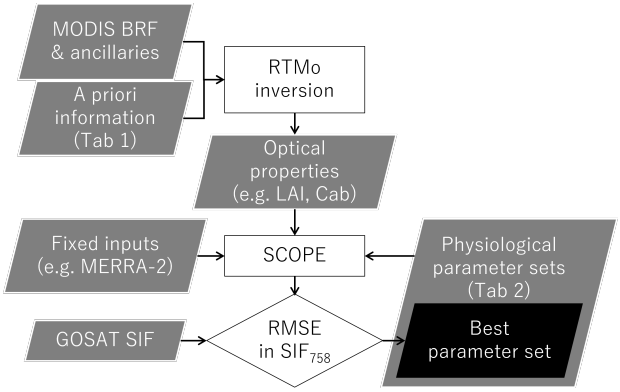

Figure 2. Schematic diagram of the model calibration procedure.

3.1 Inverting the RTMo Soil-Leaf-Canopy Radiative-Transfer Model

3.1.1 Overview and Modifications

We carried out inversion analysis to retrieve the canopy structural, leaf optical, and soil parameters of the grassland. The optical radiative transfer model (RTMo) is a submodule of the SCOPE model. It is composed of the PROSPECT leaf model (Jacquemoud & Baret, 1990), the 4SAIL canopy model (W. Verhoef, 1998), and the BSM soil model (Yang et al., 2020). The inversion algorithm based on RTMo (van der Tol et al., 2016; W. Verhoef et al., 2018) enables retrieval of the parameters from TOC spectral reflectance (400–2400 nm). We used the RTMo retrieval code version itc2020 with the Optipar2017_ProspectD library. This library was also used in the forward simulation. The RTMo parameters were retrieved from the MODIS bidirectional reflectance factor (BRF) (Lyapustin & Wang, 2018) by convolving with its spectral response function.

We have modified the RTMo retrieval code as follows.

1. While the original code retrieves the parameters from the TOC hemispherical-directional reflectance factor or top-of-atmosphere radiance, we modified it to enable retrieval from TOC BRF to use the MODIS BRF data.

2. The original code assumes a horizontally homogeneous canopy, which is generally invalid at the $>$ 1-km scale, especially for sparse vegetation in drylands. Therefore, we introduced fractional vegetation cover (FVC) as a new canopy structural parameter to adjust landscape-level clumping. Linear spectral mixing of vegetated and nonvegetated lands was assumed as in the literature (e.g., Weiss & Baret, 2016).

3. We implemented procedures to calculate model parameter errors (Rodgers, 2000) used in the optimization process in the Bayesian inversion to avoid overfitting to observed reflectance

and improve retrieval robustness (detailed in Text S2).

3.1.2 Retrieval Procedure

The cost function χ^2 of the RTMo retrieval is based on a Bayesian inversion approach,

$$\chi^2 = \sum_{i=1}^{n} \left(\frac{R_i^{\mathrm{obs}} - R_i^{\mathrm{mod}}(\mathbf{x})}{\sigma_{\epsilon,\ i}} \right)^2 + \sum_{j=1}^{m} \left(\frac{x_j - \mu_j}{\sigma_{a,j}} \right)^2, \quad (1)$$

where R_i is the reflectance in the ith bands of a spectroradiometer (MODIS BRF here, $n = 12$); superscripts designate observation (obs) and RTMo (mod). $_{\epsilon}$ denotes the root-sum-square of instrumental noise and model uncertainty (Eq. S1). denotes the a priori values, and $\mathbf{x}$ denotes the RTMo parameters to be retrieved. The uncertainty (i.e., standard deviation) $_{a}$ of the a priori values was set to the default or quantified by assuming uniform probability distributions as in W. Verhoef et al. (2018) (but based on the strict definition here; $\sigma_a^2 = \int_{\mathrm{LB}}^{\mathrm{UB}} \frac{(x-\mu)^2}{UB-LB} \mathrm{dx}$). Tables 1 and S1 summarize the settings. Minimization of the cost function (Eqs. 1 & S1) was iteratively solved using the trust-region-reflective method. The posterior uncertainty $_{p} = \left[\sigma_{p,1}, \sigma_{p,2}, \ldots, \sigma_{p,m}\right]^T$ can be expressed as

$$\left[\sigma_{p,1}^2, \sigma_{p,2}^2, \ldots, \sigma_{p,m}^2\right]^T = \mathrm{diag}\left[\left(\mathbf{K}^T \mathbf{S}_{\epsilon}^{-1} \mathbf{K} + \mathbf{S}_a^{-1}\right)^{-1}\right], \quad (2)$$

where $\mathbf{S}_{\epsilon}$ and $\mathbf{S}_a$ are the (diagonal) covariance matrices of the measurement error and the priori uncertainty, respectively (the diagonals are $\sigma_{\epsilon,i}^2$ and $\sigma_{a,j}^2$, respectively), and $\mathbf{K} = \frac{\partial \mathbf{R}}{\partial \mathbf{x}}$ is the Jacobian matrix. The values of $_{p}$ depend on the assumptions in $\mathbf{S}_a$ but provide insights into which retrievals are more strongly constrained by observation.

Table 1. *Retrieval Settings for Vegetation Parameter Estimation.*

	Definition	Unit	μ	σ_a	LB	UB
B	Soil brightness	[-]	0.45	0.26	0	0.9
BSMlat	Dry soil spectral shape	[-]	28^{*1}	4^{*1}	-	-
BSMlon		[-]	56^{*1}	4^{*1}	-	-
SMC	Volumetric water content in surface soil	[vol%]	MERRA-2	5^{*2}	-	-
Cab	Chlorophyll a + b content	[µg cm^{-2}]	15^{*3}	45	0	100
Cca	Carotenoid content	[µg cm^{-2}]	$f(Cab)$ ^{*4}	4	0	25
Cant	Anthocyanin content	[µg cm^{-2}]	0	1	-	-
Cdm	Dry matter content	[g cm^{-2}]	0.005	0.008	0	0.02
Cw	Equivalent water thickness	[cm]	0.01	0.02	0	0.05
Cs	Brown pigments content	[-]	0.1	1.4	0	2.5^{*5}

	Definition	Unit	μ	σ_a	LB	UB
N	Leaf structure parameter	[-]	1.4	1	-	-
$\boldsymbol{LAI}$	Leaf area index	[m^2 m^{-2}]	MCD15 C6	*6	0	7
LIDFa	Average leaf inclination	[-]	-0.5*7	0.76	-	-
LIDFb	Bimodality of the leaf angle distribution	[-]	-0.5*7	0.76	-	-
$\boldsymbol{FVC}$	Fractional vegetation cover	[m^2 m^{-2}]	MOD44 C6	0.1*8	0	1

Note: μ is the a priori mean, σ_a is the a priori standard deviation, and LB and UB are the lower and upper boundaries, respectively. The retrieved parameters in the vegetation parameter estimation step are shown in bold face.

*1Table S1; *2Reichle et al. (2017); *3Minimum value of green leaves defined by Weiss & Baret (2016); *4The regression line from Sims & Gamon (2002, Figure 7); *5Pacheco-Labrador et al. (2021); *6max[1/3, standard deviation of MCD15 LAI]. 1/3 is based on the 3 rule and the difference between MCD15 LAI and observed total LAI (K. Yan et al., 2016); *7Plagio-erectophile with 65° average leaf inclination (W. Verhoef, 1998); *8Climatological mean of the standard deviation of the MOD44 FVC in the study area.

The RTMo retrieval was applied to the averaged BRF within a GOSAT footprint of 10.5 km diameter, and the parameters to be retrieved were determined as follows. An example spectrum observed on 7 July 2012 is shown in Figure 3 (left); the right panels show the spectrum of the Jacobian matrix for the same datum and show clear implications. (1) It is obvious that the dominant parameter is the leaf area index (LAI), and the other parameters for the structure of the canopy or leaf ($LIDF$, FVC, and N) have similar spectral shapes, suggesting the difficulty of retrieving these parameters simultaneously. (2) The sensitivity to SMC is weak, and its spectral shape is similar to that of soil brightness (B) except for the signs. (3) The 1st- and 2nd-peak positions of the brown pigments Cs overlap with the peaks of the soil parameter $BSMlat$ and chlorophyll content Cab, respectively. Therefore, (1) we included the a priori LAI and FVC using MODIS products (MCD15A2H, Myneni et al., 2015; MOD44B, Dimiceli et al., 2015) to constrain these parameters and fix the other structural parameters, (2) we fix the SMC value to that of MERRA-2, and (3) adopt a 2-step retrieval strategy. First, for preparation, $BSMlat$ and $BSMlon$ values were retrieved using only summer data with homogeneous green cover ($LAI > 1$ and $FVC > 0.75$) by assuming $Cs = 0$. Then, we retrieved vegetation properties with fixed values of $BSMlat$ and $BSMlon$ obtained in the 1st step. The uncertainty in unretrieved parameters was explicitly considered using Eq. S1 in both steps. The root mean square error (RMSE) of the modeled spectrum in Figure 3 (left), obtained by these procedures, was 0.004; this is comparable to previous studies that used high-resolution images (e.g., Bayat et al., 2018).

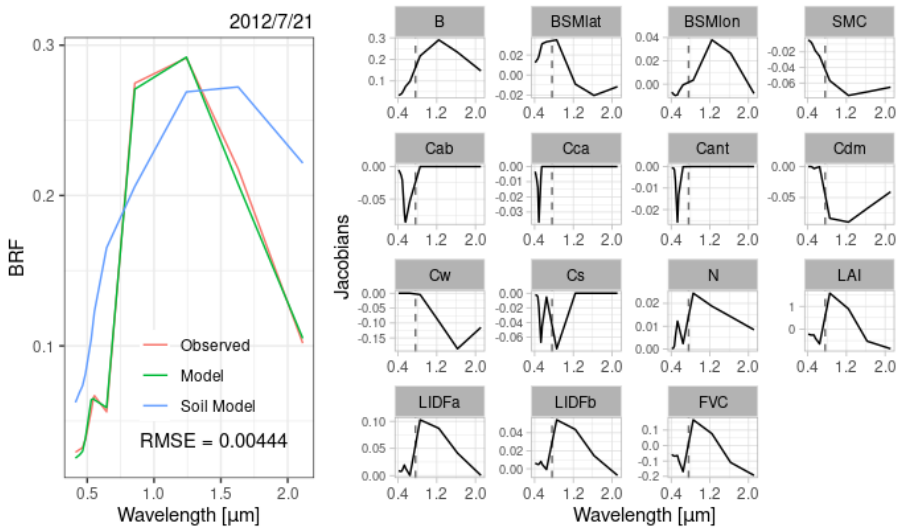

Figure 3. (left) Observed and simulated BRF spectrum for MODIS bands 1–12 on a typical summer day (LAI = 1.9 m^2 m^{-2}, Cab = 23 μg cm^{-2}). (right) The corresponding Jacobians ($\partial \frac{BRF}{\partial} x$) for each model parameter x. Dashed lines in the right panels indicate the position of the GOSAT SIF retrieval window (758 nm).

3.2 Modifications to the SCOPE Soil-Vegetation-Atmosphere Transfer Model

3.2.1 Overview and Bug Fixing

The multilayer SVAT model SCOPE can predict spectral and directional radiative transfer, including the emissions of SIF (van der Tol et al., 2019) and thermal infrared radiation. We used the latest version, SCOPE2.1. This model has two options for the photosynthesis-fluorescence scheme, TB12 and MD12, and we used the latter because of its more process-based nature (Mohammed et al., 2014). The MD12 scheme is composed of the photosynthesis model of Farquhar et al. (1980) and the MD12 quantum yield parametrization (Dayyoub, 2011) as follows:

$$\Phi_F = \min\left[\Phi_F^{\mathrm{PQ}}, \Phi_F^{\mathrm{NPQ}}\right], \quad (3)$$

$$\Phi_F^{\mathrm{NPQ}} = \Phi_P \frac{k_F}{k_{\mathrm{PSII}}} \frac{1}{q_{\mathrm{Ls}} - \frac{J_a}{J_{\mathrm{max}}}}, \quad (4)$$

where Φ_F and Φ_P are quantum yields of fluorescence [superscripts designate photochemical (PQ) and nonphotochemical quenching (NPQ)] and photochemistry, respectively. Under moderate- to high-light conditions expected at satellite

overpass times, plants are generally in the 'NPQ-phase' (Magney et al., 2020). k is the rate constant [fluorescence (F) and the intrinsic (i.e., fully open and functional) rate of photosystem II (PSII)], the values of which were adopted from Thum et al. (2017). q_{Ls} is the fraction of the functional reaction center (= 0.95 in this study), J_{max} is the maximum electron transport rate, and J_{a} is the actual electron transport rate under the colimitation with the carboxylation rate. Φ_{P} is a function of J_{a} and the PAR absorbed by chlorophylls, and the values of J_{a} and J_{max} are predicted by the photosynthesis model; the J_{max} value at 25 °C was determined from the maximum carboxylation rate V_{cmax} using the empirical relationship derived by Leuning (1997). Additional details are provided in Thum et al. (2017).

We found the following issues in SCOPE2.1 that can lead to significant errors in drylands. The first two were reported by Dutta et al. (2019) and have been fixed in the TB12 scheme since v1.73; however, they remain in the MD12 scheme.

1. The iteration to converge intercellular CO_2 concentration is omitted in MD12, which eliminates the minimum stomatal conductance (g_0).
2. An exponential Q_{10} function was still used in MD12 to express the effect of leaf temperature on respiration, which results in a steep decrease in stomatal conductance under hot conditions.

In this study, we fixed the above along with the implementations in TB12. In addition, we found two other issues.

1. The density of air $_{\mathrm{a}}$ is fixed to 1.2047 kg m^{-3} (i.e., dry air at 20 °C and 101 kPa).
2. Leaf boundary layer resistance is implicitly neglected since v2.1.

A third issue is simple but significant in regions at high altitudes and a non-temperate climate (e.g., the Mongolian Plateau); this results in large bias in the leaf temperature because sensible and latent heat fluxes are proportional to $_{\mathrm{a}}$. A fourth issue is that the leaf temperature is forced close to the air temperature, resulting in bias, diminishing heat stress and exaggerating stomatal control, especially in grasslands (Jarvis & McNaughton, 1986).

After fixing these issues, we further modified SCOPE2.1 to adequately evaluate GPP and SIF signals in semiarid grasslands. We present an outline of the modified code below. Table 2 summarizes the parameter settings, including the newly implemented settings.

Table 2. *Primary Parameter Settings in SVAT Simulation.*

	Definition & Unit	
Aerodynamics and Canopy Geometry		
d	Zero-plane displacement height [m]	~0.4 in sum

	Definition & Unit	
z_o	Roughness length for momentum [m]	$f(d, LAI)$ [*2]
h_c	Canopy height [m]	$f(d, LAI)$ [*2]
l_w	Leaf characteristic length [m]	0.04
CO_2/H_2O Exchange		
V_{cmax}	Maximum carboxylation rate at 25 °C [µmol m^{-2} s^{-1}]	{20, 80, 20}
k_V	Decaying coefficient for vertical V_{cmax} distribution [-]	$f(V_{cmax})$ [*3]
T_{year}	Growth temperature (Kattge & Knorr, 2007) [°C]	30
$\boldsymbol{g_{1M}}$	Medlyn slope parameter [$kPa^{1/2}$]	{4.61, 5.89,
g_0	Minimum stomatal conductance [mol (H_2O) m^{-2} s^{-1}]	0.01
$\boldsymbol{\theta_c}$	SMC at which $V_{cmax,app}$ starts to decrease [vol%]	{14, 18, 1}
$\boldsymbol{\theta_w}$	SMC at which $V_{cmax,app}$ becomes zero [vol%]	{8, 14, 2}
Fluorescence		
f_{qe}	Fluorescence yield at dark-adopted conditions [-]	0.012[*5]
q_{Ls}	Fraction of functional reaction centers [-]	0.95[*6]
k_{NPQs}	Rate constant of sustained NPQ [-]	0
Soil		
I	Thermal inertia [J m^{-2} $s^{-1/2}$ K^{-1}]	620
θ_{sat}	Porosity [vol%]	45.3
ψ_{sat}	Air entry hydraulic head [cm]	9.9[*7]
$\boldsymbol{b}$	Clapp-Hornberger parameter [-]	1.92[*7]

Note: Newly added variables from SCOPE2.1 are shown in bold face. Search ranges for the values of V_{cmax}, g_{1M}, θ_c, and θ_w are shown in brackets.

[*1]Not assimilated, from GEOS-5; [*2]Equations 5.125–127 of Lawrence et al. (2020); [*3]Lloyd et al. (2010); [*4]The 95% CI range for C3 grassland from de Kauwe et al. (2015, Table 1); [*5]Thum et al. (2017); [*6]The value in summer, most unstressed conditions; [*7]Converted from the values of van Genuchten parameters in the study area using the relationship proposed by Rawls et al. (1992).

3.2.2 Introducing the Drought Stress Function

Wilting reduces the mesophyll conductance of CO_2 diffusion, which apparently (temporary) reduces V_{cmax} (Zhou et al., 2013). Because SCOPE2.1 does not predict this phenomenon, we expressed it by multiplying a piecewise-linear function by V_{cmax} (hereafter, V_{cmax} denotes the values under wet conditions),

$$V_{cmax,app} = V_{cmax} \bullet max\left[\min\left[\frac{\theta-\theta_w}{\theta_c-\theta_w}, 1\right], 0\right]. \quad (5)$$

The predictions of the SCOPE model, such as the surface energy balance and the values of GPP and SIF, were calculated using the apparent value $V_{cmax,app}$.

Here, is the volumetric water content of the rhizosphere, and we assumed it is identical to the MERRA-2 surface SMC ($_{5\mathrm{cm}}$) and *SMC* in RTMo. The empirical parameters $_{\mathrm{c}}$ and $_{\mathrm{w}}$ are linked with the soil-plant hydraulic system properties, but we used Eq. 5 for brevity; note that the SCOPE model has no hydrological module. We assumed that SMC affects SIF through J_{a} and Φ_{P} (Eqs. 3–4) but does not affect $J_{\max}$ since Eq. 5 was used to express mesophyll diffusion. This nonstomatal limitation parametrization is in line with the observed weak relationship between SIF and stomatal closure (Magney et al., 2020).

In addition, we replaced the Ball-Berry stomatal conductance model used in SCOPE2.1 with the model of Medlyn et al. (2011) because the relative humidity-based Ball-Berry model is too sensitive to atmospheric aridity (see Paschalis et al., 2017, for example).

3.2.3 Replacing the Models of Aerodynamic Resistance and Soil Evaporation

We also replaced the submodels of aerodynamic resistance and soil evaporation used in SCOPE2.1 with those used in the Community Land Model version 5 (CLM5; Lawrence et al., 2020) for the following reasons.

- In addition to the issue with the leaf boundary layer, the SCOPE model does not predict the boundary layer resistance for the soil surface. Furthermore, the SCOPE model neglects large-eddy mixing in the convective boundary layer, while CLM5 considers it through a parametrization using the Deardorff velocity.
- Although a parametrization of soil surface resistance for evaporation (vapor diffusion in soil pore space) is implemented in SCOPE2.1, it only depends on the SMC and does not consider physical fundamentals such as the soil porosity and temperature. The dry surface layer model used in CLM5 considers all these fundamentals.

Since both SCOPE and CLM5 explicitly calculate the energy balance of the soil surface, we were able to introduce these submodels in a manner compatible with CLM5. See Chapter 5 of the CLM5 documentation (Lawrence et al., 2020) for details.

4 Data Processing

4.1 GOSAT SIF

We used the SIF data from GOSAT obtained during 2009–2018. The relatively long record and high accuracy of GOSAT SIF, which has been previously verified (Oshio et al., 2019; Doughty et al., 2022), are preferable to evaluate dryland interannual dynamics. The data processing used here was basically the same as in Oshio et al. (2019), but the data-filtering thresholds were modified as described in Text S3. We used the L1B product, radiance data, version V201.202 of the Thermal And Near infrared Sensor for carbon Observation – Fourier Transform

Spectrometer (TANSO-FTS) onboard GOSAT and retrieved SIF from a spectral window of 756.0–759.1 nm using the spectral fitting method (Frankenberg & Berry, 2018). Since the location of GOSAT observational points depends on the period, we selected the observations with 100% grassland in the IGBP land cover and $< 15\%$ woodland cover in MOD44B. Approximately 20–60 observations per month were obtained after filtering and screening.

To interpret the observed SIF radiance F [W m^{-2} nm^{-1} sr^{-1}] at a retrieval wavelength (758 nm here), an expression analogous to Monteith's light-use efficiency model is frequently adopted (Frankenberg & Berry, 2018):

$$\mathrm{F}(\lambda) = I_{\mathrm{PAR}} \bullet f_{\mathrm{PAR}} \bullet \varepsilon_F(\lambda) \bullet f_{\mathrm{esc}}(\lambda), \quad (6)$$

where I_{PAR} is the TOC irradiance in the PAR, f_{PAR} is the fraction of the PAR absorbed by green leaves, $_{\mathrm{F}}$ is the SIF-emission efficiency ($\propto \Phi_F$), and f_{esc} is the fraction of SIF escaping from the canopy. The SIF yield ($= \frac{\varepsilon_F \bullet f_{\mathrm{esc}}}{\pi}$) is commonly used to remove the contribution of APAR ($= I_{\mathrm{PAR}} \bullet f_{\mathrm{PAR}}$). The corresponding APAR value to the GOSAT SIF was obtained from the MODIS f_{PAR} (MCD15A2H, averaged within each GOSAT footprint) and the MERRA-2 I_{PAR} (0.5° lat $\times$ 0.625° lon) at 13:30 local time (LT) (the overpass time of GOSAT) of the same day as the GOSAT observations.

4.2 Experimental Setups and SIF-based Calibration of the SCOPE Model

Three experiments were conducted to demonstrate model improvement. The control (CTRL) run was based on the modified SCOPE model with $V_{\mathrm{cmax}} = 60$ µmol m^{-2} s^{-1}, the Medlyn slope parameter $g_{1\mathrm{M}} = 5.25$ kPa$^{1/2}$ (typical values for C3 grass; Table 2), and the well-watered assumption. The 'SCOPE2.1' run was based on the original code with almost the same parameter values as the CTRL run; the Ball-Berry slope $g_{1\mathrm{B}}$ was set to 9 [unitless]. The ZEXP run is a virtual 'zero thermal expansion' simulation; the settings are the same as the CTRL run except convection was turned off (both the Monin-Obukhov stability correction and convective boundary layer mixing), and $_{\mathrm{a}} = 1.2047$ kg m^{-3} was fixed as the original code.

The benefit of constraining SIF for GPP estimation was tested using the modified model. Four physiological parameters (V_{cmax}, $_{\mathrm{c}}$, $_{\mathrm{w}}$, and $g_{1\mathrm{M}}$) were calibrated by minimizing the RMSE of SCOPE SIF from GOSAT SIF through a grid search. The search ranges of parameters were determined based on the settings for C3 grasslands in ESMs (Table 2). First, V_{cmax} and $g_{1\mathrm{M}}$ values were calibrated using wet data ($_{5\mathrm{cm}} > 19$ vol%). Calibration was separately conducted for June–August (JJA) and the remainder of the year to distinguish drought impacts from phenology. The run using the best parameter set was named the calibrated (CAL) run.

4.3 Forcing and Benchmarking Datasets

The modified and original SCOPE models were forced by MERRA-2 meteorology at the 10-m height and the atmospheric CO_2 concentration at the surface-pressure level obtained from the GOSAT L4B product version V02.07. The spectral shape of the TOC irradiance was fixed to the default (FLEX-S3_std.atm), and broadband MERRA-2 irradiance data were used to scale the magnitude; the direct and diffuse components were separately scaled by making a minor modification to the code. Continuous 16-hour simulations during the daytime were conducted for each GOSAT observation because accurate ground heat flux calculations require a soil temperature history. We used the retrieved RTMo parameters but replaced the uncertain *Cab* data ($_{\mathrm{p}} > 20$ µg cm^{-2}) with its monthly mean value.

The performance of the models was evaluated by comparison with the MERRA-2 latent heat flux of evapotranspiration ($\mathrm{lE}_{\mathrm{total}}$), the MODIS land surface temperature (LST) (MYD11A1, Wan et al., 2015), and the MODIS GPP (MYD17A2H, Running et al., 2015). Since the study area has sparse vegetation, we adopted a 'mosaic' approach; a total surface flux was evaluated as a weighted sum of the fluxes from vegetated and nonvegetated surfaces weighted by FVC.

5 Results

5.1 Observed Seasonal and Interannual Dynamics

Figure 4 shows the 10-year time series of MERRA-2 meteorology and satellite data (MODIS LAI and FVC, and GOSAT SIF). The monthly means of the cloud fraction within the field of view of the GOSAT FTS were $< 20\%$ in general (Figure 4d), and the monthly means of SIF_{758} approached zero in winter, almost within the margin of the 90% confidence interval (CI), except in February 2010 and 2015. These results supported data consistency and quality during the growing season.

The monthly means of the 2-m air temperature fall below 0 °C for approximately half of the years, and most precipitation falls during short periods in summer (Figure 4a). The precipitation showed large interannual variations, and the SMC decreased in early summer in 2011, 2016, 2017, and 2018 when precipitation was delayed (Figure 4b). On a monthly basis, the precipitation was strongly correlated with the MODIS LAI ($r = 0.90$), and the LAI was strongly correlated with the SIF ($r = 0.76$). However, even when the LAI did not decrease, the SIF dropped below 0.15 mW m^{-2} nm^{-1} sr^{-1} when the mean SMC among GOSAT footprints fell below 15–16 vol%, for example, in August 2010, June 2013, July 2016, and July 2017.

There is no clear relationship between the SIF values and the phase angle $_{\mathrm{GOSAT}}$ (i.e., hot spot). However, this does not mean surface homogeneity, as seen by large variations in the MODSI FVC values (Figure 4c); the FVC values dropped below 50% frequently in 2014 and 2018.

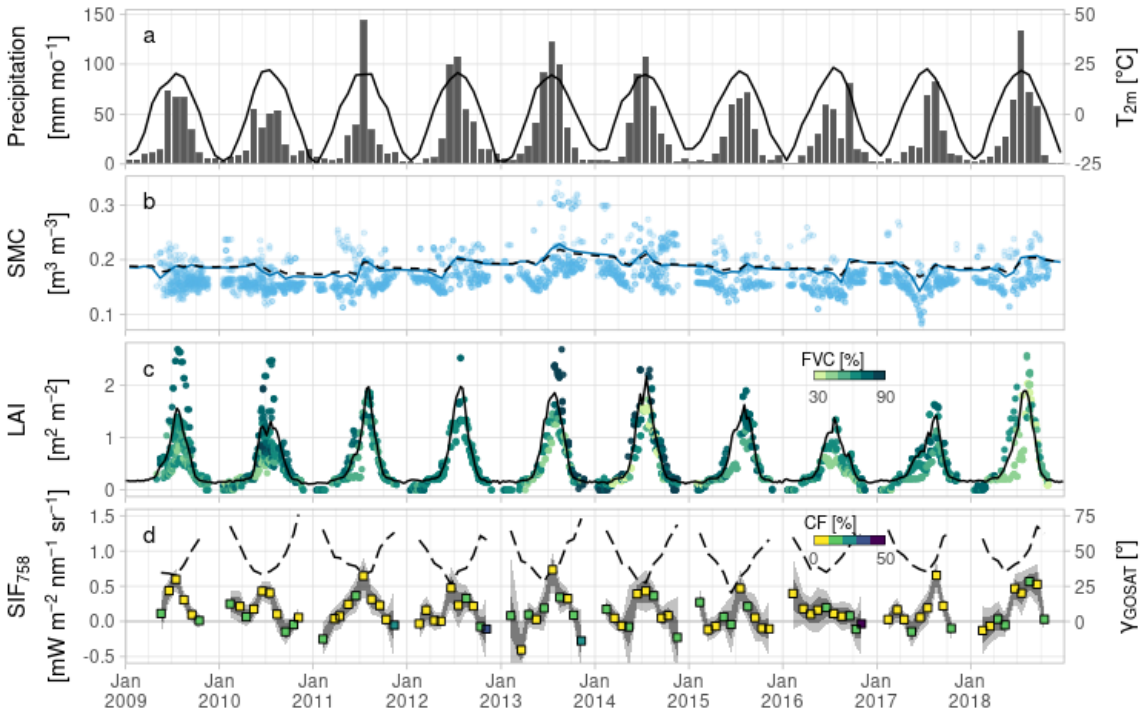

Figure 4. (**a**, **b**) Time series of MERRA-2 meteorology and (**c**) MODIS LAI and FVC, representing the mean quantities within each GOSAT footprint (circles) and within the grassland in the study area boundary (bars and lines): precipitation (bars in **a**), monthly mean air temperature T_{2m} (line in **a**), and predawn SMC at depths of 0–5 cm (blue symbols in **b**) and 10–100 cm (dashed line in **b**). (**d**) Monthly means of GOSAT SIF_{758} (squares) and ancillary data: dark and light shades indicate the standard error and the 90% CI of the SIF, respectively; colors in squares indicate the cloud fraction (CF) in the field of view; and dashed lines indicate the phase angle γ_{GOSAT}.

5.2 Inversion Results and Justification of the Forward Model

Among the three modifications to the RTMo retrieval code, the introduction of FVC had the largest impacts on retrievals. When FVC was neglected (i.e., $FVC = 1$ is fixed), this bias was compensated by underestimation in LAI and Cab (see the Jacobian in Figure 3), and the values of Cab dropped below 10 g cm^{-2} in most cases (Figure S2).

Figure 5 shows the inversion results using the modified RTMo retrieval code. The RMSE in the modeled BRF increased in winter (not shown) and ranged from 0.0025 to 0.0287. The retrieved values of LAI and FVC are higher than those of the a priori MODIS products in general (Figures 5a–b); the increase in LAI was remarkable in low-LAI cases. The LAI results were expected since

the MODIS algorithm retrieves green LAI (K. Yan et al., 2016), whereas RTMo retrieves the total LAI, including brown leaves. All the retrieved LAI values fall within the range of ± 1 m^2 m^{-2} from the priors. Figures 5c–d show the time series of the retrieved chlorophyll content *Cab* and brown pigments *Cs*, respectively (see Figure S3 for *Cw* and *Cdm*). They exhibit clear seasonality, and the *Cab* values reach 20–40 g cm^{-2} in summer and do not clearly decrease in the drought years of 2015–2017. In general, the retrieved *Cs* shows the opposite phase to that of *Cab*.

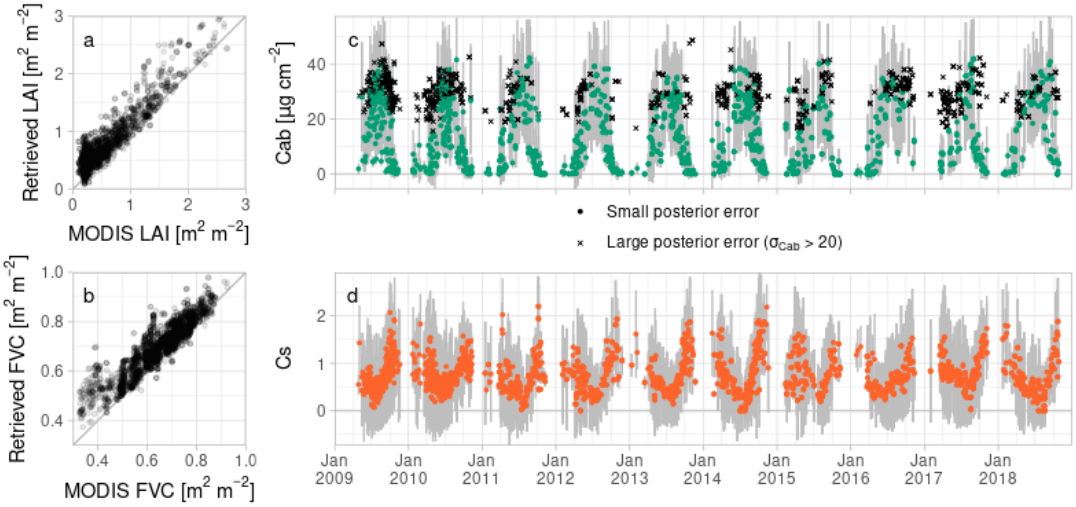

Figure 5. (**a**, **b**) Comparison between the a priori (MODIS products) and the a posteriori values for LAI and FVC. (**c**, **d**) Time series of the retrieved chlorophyll content *Cab* and brown pigments *Cs*. Error bars indicate the standard deviation of the a posteriori values.

Using these 10-year retrievals, the f_{esc} at 758 nm was predicted by the SCOPE model (Figure 6). The f_{esc} decreased from 0.55 to 0.2 with the increase in *Cs*, which strongly absorbs 758-nm SIF (Figure 3). Higher LAI (i.e., fewer canopy gaps) increases the canopy interceptance of photons, but the relationship between LAI and f_{esc} was not clear in the grassland.

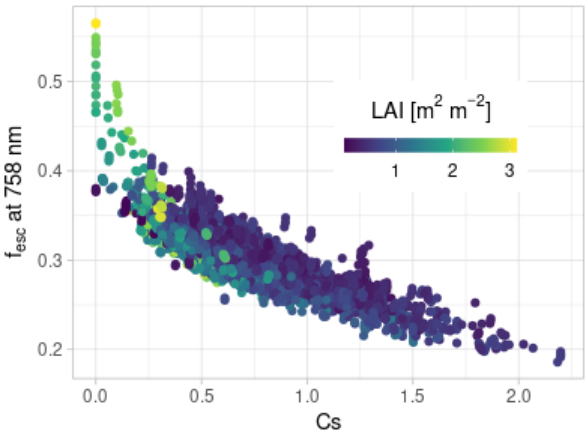

Figure 6. Simulated escape ratio f_{esc} at 758 nm for GOSAT observations throughout the study period and the relationships to retrieved *Cs* and LAI.

Figure 7a shows the evapotranspiration difference between the modified and original models. The SCOPE2.1 run substantially overestimated $\mathrm{lE}_{\mathrm{total}}$ compared with MERRA-2 ($r = 0.60$, mean bias = +129 W m^{-2}), while the CTRL run tracked it better ($r = 0.85$, mean bias = +30 W m^{-2}). Figures 7c–d show diurnal changes in the simulated SIF_{758} and canopy average temperature $\mathrm{T}_{\mathrm{c,ave}}$ on a calm summer day (23 July 2010). The CTRL run predicted a monotonic peak in SIF_{758}, whereas the SCOPE2.1 and ZEXP runs predicted clear midday depression. At the time of the GOSAT overpass (13:30 LT), the SIF_{758} value in the CTRL run reached 250% of the prediction by SCOPE2.1. This substantial difference results from the canopy temperature; the peak value of $\mathrm{T}_{\mathrm{c,ave}}$ around noon was ~35 °C in the CTRL run, whereas it reached ~50 °C in the other two runs. Some of these differences are caused by aerodynamic resistance, as shown in Figure 7b. The above-canopy aerodynamic resistance in SCOPE2.1 (gray circles) steeply increased when the 10-m horizontal wind speed dropped below 2 m s^{-1}, whereas the CTRL run predicted more stable changes.

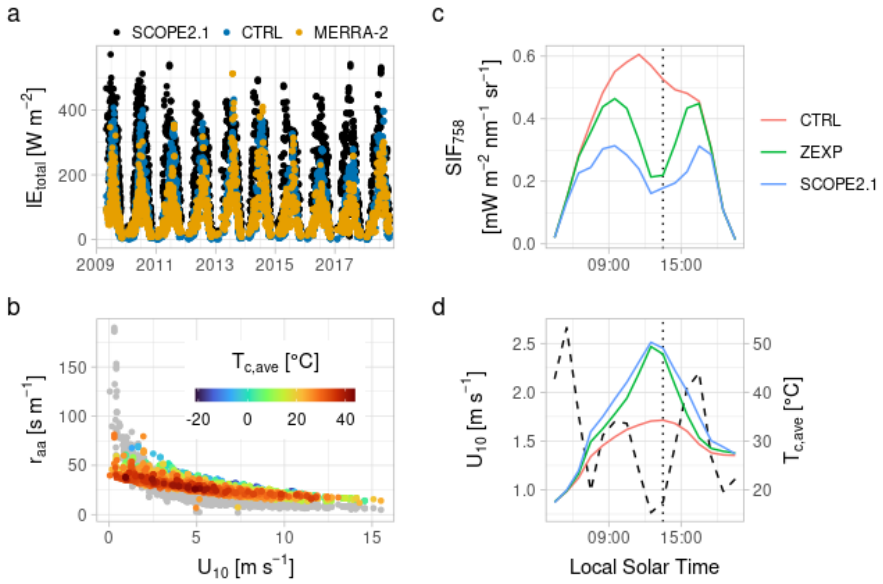

Figure 7. Model comparison results. (**a**) The latent heat of evapotranspiration lE_{total} at 13:30 LT throughout the study period. (**b**) Relationship between above-canopy aerodynamic resistance r_{aa} and 10-m horizontal wind speed U_{10} at 13:30 LT. Gray and colored circles indicate the results from the original model (SCOPE2.1) and the control (CTRL) run, respectively. (**c**, **d**) Diurnal patterns of nadir-view SIF_{758} (**c**), U_{10} (dashed line in **d**), and average canopy temperature $T_{c,ave}$ (continuous lines in **d**) for the CTRL, ZEXP (zero thermal expansion) and SCOPE2.1 runs (see Sect 4.2) on a calm summer day (23 July 2010). Vertical dotted lines indicate the overpass time of GOSAT (13:30 LT).

5.3 Drought Impacts on SIF and GPP

Figure 8 shows the relationships between GOSAT SIF and SMC, considering APAR as a controlled variable. The SIF increased with APAR, while its slope (= SIF yield) increased with $_{5cm}$ (Figure 8a); the threshold of $_{5cm}$ = 15.4 vol% resulted in the largest difference between the SIF yields obtained under dry- and wet-SMC conditions. The mean ± standard error [10^{-6} nm^{-1} sr^{-1}] of the SIF yields were 2.78 ± 0.14 (wet) and 2.09 ± 0.21 (dry). Furthermore, the monthly means of the SIF yield and $_{5cm}$ show a nonlinear pattern (Figure 8b). Although the SIF-yield values have large errors, the smoothing curve for the throughout 10-year data depicts a clear sigmoidal pattern, which is characteristic of wilting. There is no clear relationship between this SMC-associated change and *Cab* values.

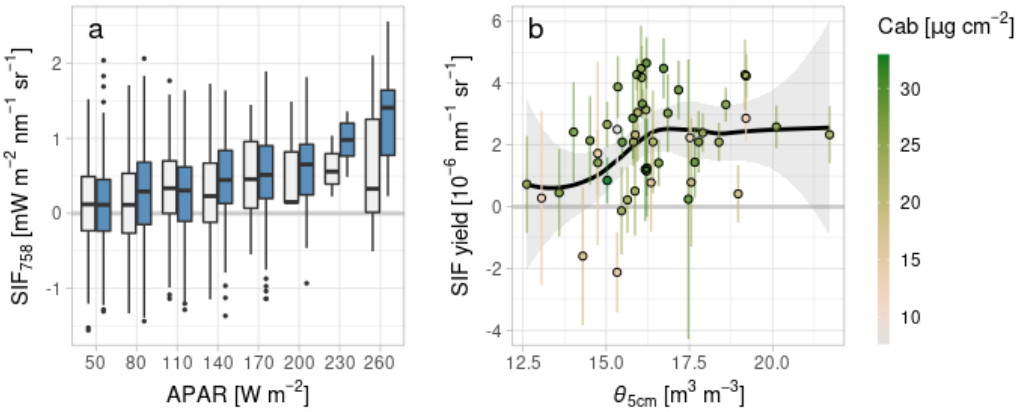

Figure 8. (**a**) Box-whisker plot of GOSAT SIF against APAR binned at 30 W m^{-2} intervals. Blue and white boxes indicate the data with $\theta_{5cm} > 15.4$ vol% and < 15.4 vol%, respectively. (**b**) Relationship between monthly means of SIF yield and θ_{5cm}. Error bars indicate the standard error. The smoothing curve is the local regression; the smoothing span was determined by 5-fold cross-validation that minimizes RMSE within a range that produces a monotonic relationship of SIF yield and θ_{5cm}. The shading indicates the 95% CI.

The model calibration was conducted through a series of forty-four 10-year simulations. The best parameter set was found to be $V_{\mathrm{cmax}} = 60$ (JJA) and 20 (other) µmol m^{-2} s^{-1}, $g_{1\mathrm{M}} = 4.61$ kPa$^{1/2}$, $_{\mathrm{c}} = 16$ vol%, and $_{\mathrm{w}} = 10$ vol% [RMSE = 0.754, mean bias = 0.004 mW m^{-2} nm^{-1} sr^{-1} (JJA)]. Notably, the modified model outperformed MERRA-2 in LST prediction when Aqua/MODIS was used as a reference. The mean bias was +1.16 K in the CAL run, +0.98 K in the CTRL run, and −4.4 K in MERRA-2.

Figure 9a shows the differences in SIF_{758} between the CTRL and CAL runs. The improvement is obvious in 2016 and 2017, whereas the CAL run slightly underestimated SIF_{758} in the summers of 2009 and 2010. The underestimation in July 2009 was statistically significant ($p < 0.05$). The predicted GPP dynamics (Figure 9b) were similar to the LAI dynamics. The mean ratio of the around-noon (13:30 LT) GPP values in the CAL run to that in the CTRL run was 73% in entire seasons and 91% in JJA, which indicates that SIF constrained GPP mostly through the tuning of phenology in V_{cmax} in ordinary years. However, in the drought years of 2016 and 2017, the ratio in JJA drops to 80% due to wilting (i.e., tuning $V_{\mathrm{cmax,app}}$). Figure 10 shows a comparison of daily GPP between the CAL run and the MYD17 MODIS product. The CAL run tended to predict larger GPP than the MODIS product; the ratio was 1.35 on average. The data are scattered around the line of the 1:1 relationship when GPP < ~2.5 gC m^{-2} d^{-1}, while in high-GPP cases, the CAL run predicted approximately 1.5 times the MODIS GPP (dashed line). The wilting effect in the CAL run was evident, and the predicted GPP values sometimes became zero.

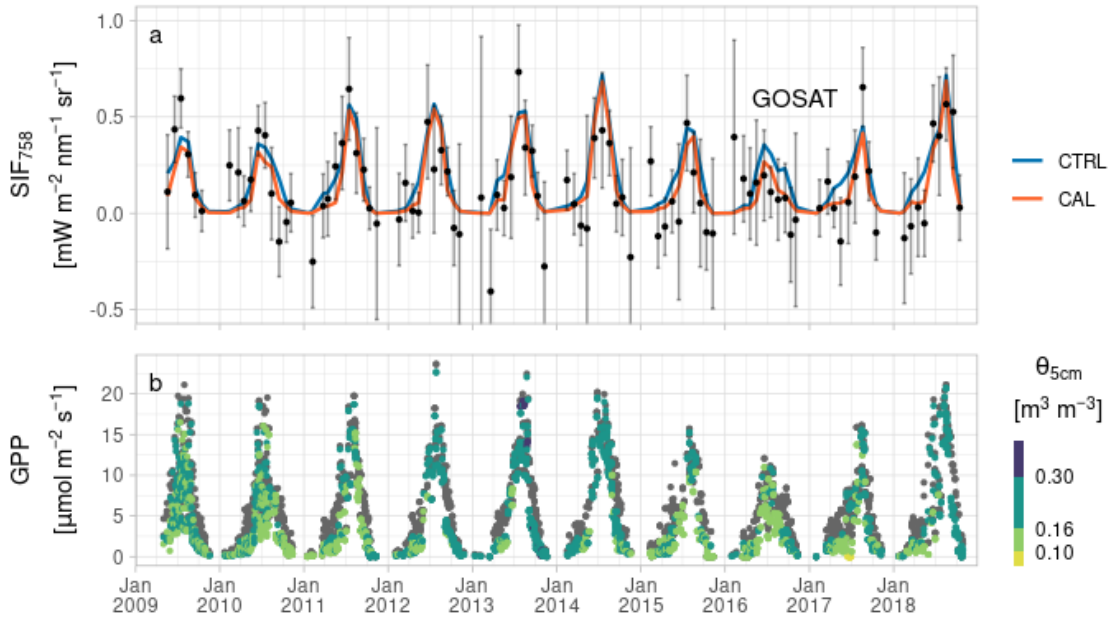

Figure 9. Comparison between uncalibrated (CTRL) and calibrated (CAL) run predictions for (**a**) SIF_{758} and (**b**) GPP at 13:30 LT. Circles and error bars in (**a**) indicate the monthly mean GOSAT SIF and its 90% CI, respectively. Gray and colored circles in (**b**) indicate the CTRL and CAL runs, respectively.

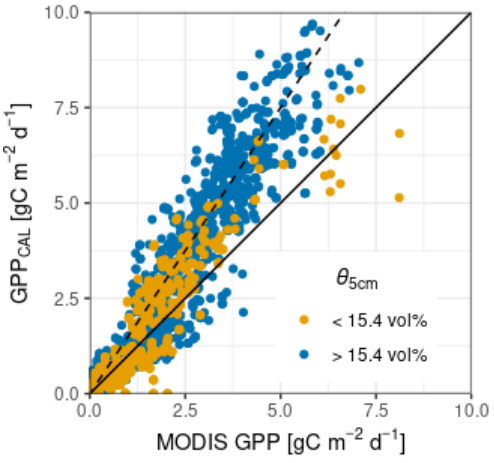

Figure 10. Relationships between simulated GPP (CAL run, see text) and the MODIS GPP. The dashed line corresponds to the estimation of Madani et al.

(2014) for the FLUXNET grassland sites across North America.

6 Discussion

6.1 Comparison with Previous Studies and Key Findings

The CAL run predicted larger GPP values than the MODIS product (Figure 10), which is partly due to the increase in LAI and FVC (Figure 5). The range of LAI increase from the a priori (< 1 m^2 m^{-2}) falls within the product's uncertainty (Table 1; K. Yan et al., 2016), which is natural since we set the a priori uncertainty based on K. Yan et al. (2016). The increase in FVC ($<$ ~10% pt) was not an expected result but is reasonable, as S. Huang & Siegert (2006) noted that MOD44B underestimated the FVC by 12.5% pt in the Mongolian Plateau compared with their on-site calibrated estimation. Note that the normalized difference vegetation index was the most influential input for the machine-learning-based MOD44B (see the algorithm document), which may indicate that the MOD44B FVC is close to the 'green fraction' rather than the vegetation fraction. The magnitude of the GPP increase (Figure 10) is also within a reasonable range compared with recent satellite GPP products calibrated to ground observations (e.g., Zheng et al., 2020). Notably, Madani et al. (2014) compared the GPP obtained from the MODIS product and the FLUXNET grassland sites across North America and reported that the tower GPP is 1.5 times as large as the MODIS GPP under unstressed conditions. This is highly consistent with our estimation.

The key findings of the present study can be summarized in three points. The first is observational evidence that GOSAT can detect the grassland wilting point (Figure 8). We found a nonlinear decrease in the GOSAT SIF when the surface SMC dropped below 15.4 vol%. The model-based analysis (i.e., estimated values of $_{\mathrm{c}}$ and $_{\mathrm{w}}$) showed that the grassland GPP started to decrease at 16 vol% SMC and became almost zero at 10 vol% SMC. These values are close to the eddy-covariance results of Li et al. (2005) conducted at a site near our study area; in that study, the net ecosystem exchange was classified according to surface SMC levels. The thresholds were >15 vol% and <10 vol%, which agrees with our estimation within ~1 vol% (~0.01 m^3 m^{-3}) SMC.

The second finding is the corroboration that the observed wilting point can be attributed to physiology (through apparent V_{cmax} as in Eq. 5) after considering changes in canopy structure and leaf optical properties. Two model studies showed that satellite SIF could potentially be linked with root distribution (Forkel et al., 2019) or the wilting point for stomata (Qiu et al., 2018). However, chlorophyll reductions and turnover (Cs) effects on f_{esc} have not been evaluated, which significantly impact SIF (van der Tol et al. 2019) but have little impact on GPP. We retrieved these properties (Figures 5 and 6) and showed that (apparent) V_{cmax} tuning further improves SIF_{758} prediction (Figure 9), which means that GOSAT SIF could provide an additional constraint on GPP that could not be derived from optical reflectance.

The third finding is the importance of surface energy balance and turbulent

transport when evaluating SIF. As shown in Figure 7, the grassland SIF predicted by SCOPE 2.1 was substantially lower than that of the CTRL run (150% error). Verma et al. (2017) also reported that SCOPE (v1.61, TB12) predicts substantially low SIF radiance compared with that retrieved by the Orbiting Carbon Observatory-2 (OCO-2) satellite in a C4 grassland (~200% error in the worst case). Considering that the CAL run reproduced the GOSAT SIF_{758} well (Figure 9a), we regard these discrepancies to be due to underestimation of the original SCOPE model and not due to bias in GOSAT and OCO-2.

6.2 Limitations and Future Implications

However, there are some uncertainties in photosynthesis-fluorescence schemes in model simulations. SIF-based retrievals of V_{cmax} attracted early attention, but up-to-date studies reported their weak relationship (e.g., Koffi et al., 2015; van der Tol et al., 2016; Verma et al., 2017; Pacheco-Labrador et al., 2019; see also the review by Frankenberg & Berry, 2018). Figures 9 and 10 apparently contradict the up-to-date studies—the key difference was the use of the MD12 scheme here, which is more sensitive to physiology than the generally used TB12 (Verrelst et al., 2015). A leaf-scale model comparison study reported that MD12 outperforms TB12 (Mohammed et al., 2014), but their performance at a larger scale is unclear because MD12 is rarely used. Another problem is the uncertainty in the fraction of functional reaction center q_{Ls} that dominate the SIF predicted by MD12 (Verrelst et al., 2015). To our knowledge, the study of Porcar-Castell (2011) is the only report of the measurement of this parameter. Care needs to be taken that all results presented here are based on $q_{\mathrm{Ls}} = 0.95$, which is adopted from the most unstressed condition in the study of Porcar-Castell (2011). The underestimation of SIF_{758} in July 2009 (Figure 9) was potentially caused by reductions in q_{Ls} (see Eq. 4), i.e., drought-induced photoinhibition (Cornic & Massacci, 1996).

The retrieved *Cab* values were scattered, as shown in Figure 5c. Although the SCOPE SIF saturates to changes in *Cab* when it exceeds ~20 µg cm^{-2} (Koffi et al., 2015), the retrieved *Cab* values dropped below this threshold frequently in the summers of 2009 and 2010. Figure 9 shows that the predicted SIF_{758} values in the CAL run moderately match those of GOSAT in 2010 but were underestimated in 2009; this may be caused by retrieval error in *Cab*. Due to this error, we cannot assert that the observed wilting pattern is definitively caused by physiology. However, this limitation results from the overlap of sensitive wavelengths between RTMo parameters (Figure 3). In other words, the limitation results from the optical nature of vegetation and soil. To increase the robustness of satellite-based GPP estimation, it is promising to combine SIF with thermal infrared radiation (e.g., Pacheco-Labrador et al., 2019) and/or X-band microwaves. LST-based GPP estimation is preferable in its insensitivity to errors in *Cab* but requires fine tuning for aerodynamic resistance, SMC, and soil heat conduction; therefore, LST complementary works with SIF. We highlight that adequate modeling of surface energy balance and turbulent transport are fundamental to the application of this multiple-constraint approach and the

evaluation of drought signals, as shown in this study.

Acknowledgments

This study was funded by the National Institute for Environmental Studies GOSAT and GOSAT-2 projects. SIF data were retrieved using the GOSAT-2 Research Computation Facility. We would like to thank Dr. Qinxue Wang at the National Institute for Environmental Studies and Prof. Jun Asanuma at University of Tsukuba for providing information about field observations in Mongolia.

Data Availability Statement

The GOSAT TANSO-FTS L1B radiance data V202.202 and L4B atmospheric CO_2 concentration data V02.07 are available via the GOSAT Data Archive Service (https://data2.gosat.nies.go.jp/) after user registration. The MODIS Collection 6 data are available via the NASA Land Processes Distributed Active Archive Center (https://lpdaac.usgs.gov/) after user registration. The MODIS spectral response function is freely available at https://oceancolor.gsfc.nasa.gov/docs/rsr/rsr_tables/. The MERRA-2 reanalysis data are available via the Goddard Earth Sciences Data and Information Services Center (https://disc.gsfc.nasa.gov/) after user registration. The global soil hydraulic property dataset (Montzka et al., 2017) is distributed under the terms of the Creative Commons Attribution 3.0 via Pangea (https://doi.org/10.1594/PANGAEA.870605). The RTMo inversion algorithm version itc2020 and the SCOPE model v2.1 are distributed under the GNU General Public License version 3 (GPLv3) and can be downloaded at https://github.com/Prikaziuk/retrieval_rtmo and https://github.com/Christiaanvandertol/SCOPE, respectively. The source code of the modified SCOPE model described in this paper is distributed under GPLv3 at https://github.com/KiyonoT/SCOPE2.1A.

References

Aarts, E., Verhage, M., Veenvliet, J. V., Dolan, C. V., & Van Der Sluis, S. (2014). A solution to dependency: Using multilevel analysis to accommodate nested data. *Nature Neuroscience*, *17*(4), 491–496. https://doi.org/10.1038/nn.3648

Badr, H. S., Zaitchik, B. F., & Dezfuli, A. K. (2015). A tool for hierarchical climate regionalization. *Earth Science Informatics*, *8*(4), 949–958. https://doi.org/10.1007/s12145-015-0221-7

Bayat, B., van der Tol, C., & Verhoef, W. (2018). Integrating satellite optical and thermal infrared observations for improving daily ecosystem functioning estimations during a drought episode. *Remote Sensing of Environment*, *209*, 375–394. https://doi.org/10.1016/j.rse.2018.02.027

Bennett, W. B., Wang, J., & Bras, R. L. (2008). Estimation of global ground heat flux. *Journal of Hydrometeorology*, *9*(4), 744–759. https://doi.org/10.1175/2008JHM940.1

Biederman, J. A., Scott, R. L., Bell, T. W., Bowling, D. R., Dore, S., Garatuza-Payan, J., et al. (2017). CO2 exchange and evapotranspiration across dryland ecosystems of southwestern North America. *Global Change Biology*, *23*(10), 4204–4221. https://doi.org/10.1111/gcb.13686

Brutsaert, W., & Sugita, M. (2008). Is Mongolia's groundwater increasing or decreasing? The case of the Kherlen River basin. *Hydrological Sciences Journal*, *53*(6), 1221–1229. https://doi.org/10.1623/hysj.53.6.1221

Cornic, G., & Massacci, A. (1996). Leaf photosynthesis under drought stress. In N.R. Baker (Ed.), *Photosynthesis and the environment. advances in photosynthesis and respiration* (vol 5, pp. 347–366). Dordrecht, Springer. https://doi.org/10.1007/0-306-48135-9_14

Dayyoub, A. (2011). *Novel techniques for the remote sensing of photosynthetic processes* (Doctral dissertation). Retrieved from Alma Digital Library (https://doi.org/10.6092/unibo/amsdottorato/3992). Bologna: University of Bologna.

De Kauwe, M. G., Kala, J., Lin, Y. S., Pitman, A. J., Medlyn, B. E., Duursma, R. A., Abramowitz, G., Wang, Y. P., & Miralles, D. G. (2015). A test of an optimal stomatal conductance scheme within the CABLE land surface model. *Geoscientific Model Development*, *8*(2), 431–452. https://doi.org/10.5194/gmd-8-431-2015

Dimiceli, C., Carroll, M., Sohlberg, R., Kim, D., Kelly, M., & Townshend, J. (2015). MOD44B MODIS/Terra Vegetation Continuous Fields Yearly L3 Global 250m SIN Grid V006 [Data set]. NASA EOSDIS Land Processes DAAC. https://doi.org/10.5067/MODIS/MOD44B.006

Doughty, R., Kurosu, T. P., Parazoo, N., Köhler, P., Wang, Y., Sun, Y., & Frankenberg, C. (2022). Global GOSAT, OCO-2, and OCO-3 solar-induced chlorophyll fluorescence datasets. *Earth System Science Data*, *14*(4), 1513–1529. https://doi.org/10.5194/essd-14-1513-2022

Dutta, D., Schimel, D. S., Sun, Y., Van Der Tol, C., & Frankenberg, C. (2019). Optimal inverse estimation of ecosystem parameters from observations of carbon and energy fluxes. *Biogeosciences*, *16*(1), 77–103. https://doi.org/10.5194/bg-16-77-2019

Farquhar, G. D., von Caemmerer, S., & Berry, J. A. (1980). A biochemical model of photosynthetic CO2 assimilation in leaves of C3 species. *Planta*, *149*(1), 78–90. https://doi.org/10.1007/BF00386231

Fisher, J. B., Lee, B., Purdy, A. J., Halverson, G. H., Dohlen, M. B., Cawse-Nicholson, K., et al. (2020). ECOSTRESS: NASA's next generation mission to measure evapotranspiration from the International Space Station. *Water Resources Research*, *56*(4), e2019WR026058. https://doi.org/10.1029/2019WR026058

Forkel, M., Drüke, M., Thurner, M., Dorigo, W., Schaphoff, S., Thonicke, K., von Bloh, W., & Carvalhais, N. (2019). Constraining modelled global vegetation

dynamics and carbon turnover using multiple satellite observations. *Scientific Reports*, *9*(1), 18757. https://doi.org/10.1038/s41598-019-55187-7

Frankenberg, C., & Berry, J. (2018). Solar induced chlorophyll fluorescence: Origins, relation to photosynthesis and retrieval. In S. Liang (Ed.), *Comprehensive remote sensing* (Vol. 3, pp. 143–162). Amsterdam: Elsevier. https://doi.org/10.1016/B978-0-12-409548-9.10632-3

Friedl, M., & Sulla-Menashe, D. (2019). MCD12Q1 MODIS/Terra+Aqua Land Cover Type Yearly L3 Global 500m SIN Grid V006 [Data set]. NASA EOSDIS Land Processes DAAC. https://doi.org/10.5067/MODIS/MCD12Q1.006

Gelaro, R., McCarty, W., Suárez, M. J., Todling, R., Molod, A., Takacs, L., et al. (2017). The modern-era retrospective analysis for research and applications, version 2 (MERRA-2). *Journal of Climate*, *30*(14), 5419–5454. https://doi.org/10.1175/JCLI-D-16-0758.1

Gruber, A., Scanlon, T., Van Der Schalie, R., Wagner, W., & Dorigo, W. (2019). Evolution of the ESA CCI Soil Moisture climate data records and their underlying merging methodology. *Earth System Science Data*, *11*(2), 717–739. https://doi.org/10.5194/essd-11-717-2019

Huang, J., Li, Y., Fu, C., Chen, F., Fu, Q., Dai, A., et al. (2017). Dryland climate change: Recent progress and challenges. *Reviews of Geophysics*, *55*(3), 719–778. https://doi.org/10.1002/2016RG000550

Huang, S., & Siegert, F. (2006). Land cover classification optimized to detect areas at risk of desertification in North China based on SPOT VEGETATION imagery. *Journal of Arid Environments*, *67*(2), 308–327. https://doi.org/10.1016/j.jaridenv.2006.02.016

Jacquemoud, S., & Baret, F. (1990). PROSPECT: A model of leaf optical properties spectra. *Remote Sensing of Environment*, *34*(2), 75–91. https://doi.org/10.1016/0034-4257(90)90100-Z

Jarvis, P. G., & Mcnaughton, K. G. (1986). Stomatal control of transpiration: Scaling up from leaf to region. In A. MacFadyen & E.D. Ford (Eds.), *Advances in Ecological Research* (Vol. 15, pp. 1–49). Amsterdam: Elsevier. https://doi.org/10.1016/S0065-2504(08)60119-1

Jonard, F., De Cannière, S., Brüggemann, N., Gentine, P., Short Gianotti, D. J., Lobet, G., et al. (2020). Value of sun-induced chlorophyll fluorescence for quantifying hydrological states and fluxes: Current status and challenges. *Agricultural and Forest Meteorology*, *291*, 108088. https://doi.org/10.1016/j.agrformet.2020.108088

Kattge, J., & Knorr, W. (2007). Temperature acclimation in a biochemical model of photosynthesis: A reanalysis of data from 36 species. *Plant, Cell and Environment*, *30*(9), 1176–1190. https://doi.org/10.1111/j.1365-3040.2007.01690.x

Koffi, E. N., Rayner, P. J., Norton, A. J., Frankenberg, C., & Scholze, M. (2015). Investigating the usefulness of satellite-derived fluorescence data in inferring gross primary productivity within the carbon cycle data assimilation system. *Biogeosciences*, *12*(13), 4067–4084. https://doi.org/10.5194/bg-12-4067-2015

Kuze, A., Suto, H., Shiomi, K., Kawakami, S., Tanaka, M., Ueda, Y., et al. (2016). Update on GOSAT TANSO-FTS performance, operations, and data products after more than 6 years in space. *Atmospheric Measurement Techniques*, *9*(6), 2445–2461. https://doi.org/10.5194/amt-9-2445-2016

Lawrence, D., Fisher, R., Koven, C., Oleson, K., Swenson, S., Vertenstein, M., et al. (2020). *CLM5 Documentation*, Retrieved from https://www.cesm.ucar.edu/models/cesm2/land/CLM50_Tech_Note.pdf. Boulder, CO: National Center for Atmospheric Research.

Lee, E.-H., & Sohn, B.-J. (2011). Recent increasing trend in dust frequency over Mongolia and Inner Mongolia regions and its association with climate and surface condition change. *Atmospheric Environment*, *45*(27), 4611–4616. https://doi.org/10.1016/j.atmosenv.2011.05.065

Leuning, R. (1997). Scaling to a common temperature improves the correlation between the photosynthesis parameters Jmax and Vcmax. *Journal of Experimental Botany*, *48*(2), 345–347. https://doi.org/10.1093/jxb/48.2.345

Li, S.-G., Asanuma, J., Eugster, W., Kotani, A., Liu, J.-J., Urano, T., et al. (2005a). Net ecosystem carbon dioxide exchange over grazed steppe in central Mongolia. *Global Change Biology*, *11*(11), 1941–1955. https://doi.org/10.1111/j.1365-2486.2005.01047.x

Lloyd, J., Patiño, S., Paiva, R. Q., Nardoto, G. B., Quesada, C. A., Santos, A. J. B., et al. (2010). Optimisation of photosynthetic carbon gain and within-canopy gradients of associated foliar traits for Amazon forest trees. *Biogeosciences*, *7*(6), 1833–1859. https://doi.org/10.5194/bg-7-1833-2010

Lyapustin, A., & Wang, Y. (2018). MCD19A1 MODIS/Terra+Aqua Land Surface BRF Daily L2G Global 500m and 1km SIN Grid V006 [Data set]. NASA EOS-DIS Land Processes DAAC. https://doi.org/10.5067/MODIS/MCD19A1.006

Magney, T. S., Barnes, M. L., & Yang, X. (2020). On the covariation of chlorophyll fluorescence and photosynthesis across scales. *Geophysical Research Letters*, *47*(23), e2020GL091098. https://doi.org/10.1029/2020GL091098

Madani, N., Kimball, J. S., Affleck, D. L. R., Kattge, J., Graham, J., Van Bodegom, P. M., et al. (2014). Improving ecosystem productivity modeling through spatially explicit estimation of optimal light use efficiency. *Journal of Geophysical Research: Biogeosciences*, *119*(9), 1755–1769. https://doi.org/10.1002/2014JG002709

Martens, B., Miralles, D. G., Lievens, H., Van Der Schalie, R., De Jeu, R. A., Fernández-Prieto, D., et al. (2017). GLEAM v3: Satellite-based land evap-

oration and root-zone soil moisture. *Geoscientific Model Development*, *10*(5), 1903–1925. https://doi.org/10.5194/gmd-10-1903-2017

Medlyn, B. E., Duursma, R. A., Eamus, D., Ellsworth, D. S., Prentice, I. C., Barton, C. V. M., et al. (2011). Reconciling the optimal and empirical approaches to modelling stomatal conductance. *Global Change Biology*, *17*(6), 2134–2144. https://doi.org/10.1111/j.1365-2486.2010.02375.x

Montzka, C., Herbst, M., Weihermüller, L., Verhoef, A., & Vereecken, H. (2017). A global data set of soil hydraulic properties and sub-grid variability of soil water retention and hydraulic conductivity curves. *Earth System Science Data*, *9*(2), 529–543. https://doi.org/10.5194/essd-9-529-2017

Myneni, R., Knyazikhin, Y., & Park, T. (2015), MCD15A2H MODIS/Terra+Aqua Leaf Area Index/FPAR 8-day L4 Global 500m SIN Grid V006 [Data set]. NASA EOSDIS Land Processes DAAC. https://doi.org/10.5067/MODIS/MCD15A2H.006

Nandintsetseg, B., Shinoda, M., Du, C., & Munkhjargal, E. (2018). Cold-season disasters on the Eurasian steppes: Climate-driven or man-made. *Scientific Reports*, *8*(1), 14769. https://doi.org/10.1038/s41598-018-33046-1

Oshio, H., Yoshida, Y., & Matsunaga, T. (2019). On the zero-level offset in the GOSAT TANSO-FTS O2 A band and the quality of solar-induced chlorophyll fluorescence (SIF): comparison of SIF between GOSAT and OCO-2. *Atmospheric Measurement Techniques*, *12*(12), 6721–6735. https://doi.org/10.5194/amt-12-6721-2019

Pacheco-Labrador, J., Perez-Priego, O., El-Madany, T. S., Julitta, T., Rossini, M., Guan, J., et al. (2019). Multiple-constraint inversion of SCOPE. Evaluating the potential of GPP and SIF for the retrieval of plant functional traits. *Remote Sensing of Environment*, *234*, 111362. https://doi.org/10.1016/j.rse.2019.111362

Pacheco-Labrador, J., El-Madany, T. S., van der Tol, C., Martin, M. P., Gonzalez-Cascon, R., Perez-Priego, O., et al. (2021). senSCOPE: Modeling mixed canopies combining green and brown senesced leaves. Evaluation in a Mediterranean Grassland. *Remote Sensing of Environment*, *257*, 112352. https://doi.org/10.1016/j.rse.2021.112352

Paschalis, A., Katul, G. G., Fatichi, S., Palmroth, S., & Way, D. (2017). On the variability of the ecosystem response to elevated atmospheric CO2 across spatial and temporal scales at the Duke Forest FACE experiment. *Agricultural and Forest Meteorology*, *232*, 367–383. https://doi.org/10.1016/j.agrformet.2016.09.003

Porcar-Castell, A. (2011). A high-resolution portrait of the annual dynamics of photochemical and non-photochemical quenching in needles of Pinus sylvestris. *Physiologia Plantarum*, *143*(2), 139–153. https://doi.org/10.1111/j.1399-3054.2011.01488.x

Qiu, B., Xue, Y., Fisher, J. B., Guo, W., Berry, J. A., & Zhang, Y. (2018). Satellite chlorophyll fluorescence and soil moisture observations lead to advances in the predictive understanding of global terrestrial coupled carbon-water cycles. *Global Biogeochemical Cycles*, *32*(3), 360–375. https://doi.org/10.1002/2017GB005744

Rawls, W. J., Ahuja, L. R., Brakensiek, D. L., & Shirmohammadi, A. (1992). Infiltration and soil water movement. In D. R. Maidment (Ed.), *Handbook of Hydrology* (pp. 5.1–5.51), New York, NY: McGraw-Hill.

Reichle, R. H., Draper, C. S., Liu, Q., Girotto, M., Mahanama, S. P. P., Koster, R. D., & De Lannoy, G. J. M. (2017). Assessment of MERRA-2 land surface hydrology estimates. *Journal of Climate*, *30*(8), 2937–2960. https://doi.org/10.1175/JCLI-D-16-0720.1

Rodgers, C. D. (2000). *Inverse methods for atmospheric sounding: Theory and practice*. Singapore: World Scientific. https://doi.org/10.1142/3171

Rogers, A. (2014). The use and misuse of Vc,max in Earth System Models. *Photosynthesis Research*, *119*(1–2), 15–29. https://doi.org/10.1007/s11120-013-9818-1

Rogers, A., Medlyn, B. E., Dukes, J. S., Bonan, G., von Caemmerer, S., Dietze, M. C., et al. (2017). A roadmap for improving the representation of photosynthesis in Earth system models. *New Phytologist*, *213*(1), 22–42. https://doi.org/10.1111/nph.14283

Running, S. W., Mu, Q., & Zhao, M. (2015). MYD17A2H MODIS/Aqua Gross Primary Productivity 8-Day L4 Global 500m SIN Grid V006 [Data set]. NASA EOSDIS Land Processes DAAC. https://doi.org/10.5067/MODIS/MYD17A2H.006

Sims, D. A., & Gamon, J. A. (2002). Relationships between leaf pigment content and spectral reflectance across a wide range of species, leaf structures and developmental stages. *Remote Sensing of Environment*, *81*(2–3), 337–354. https://doi.org/10.1016/S0034-4257(02)00010-X

Stocker, B. D., Zscheischler, J., Keenan, T. F., Prentice, I. C., Seneviratne, S. I., & Peñuelas, J. (2019). Drought impacts on terrestrial primary production underestimated by satellite monitoring. *Nature Geoscience*, *12*(4), 264–270. https://doi.org/10.1038/s41561-019-0318-6

Thum, T., Zaehle, S., Köhler, P., Aalto, T., Aurela, M., Guanter, et al. (2017). Modelling sun-induced fluorescence and photosynthesis with a land surface model at local and regional scales in northern Europe. *Biogeosciences*, *14*(7), 1969–1984. https://doi.org/10.5194/bg-14-1969-2017

Trugman, A. T., Medvigy, D., Mankin, J. S., & Anderegg, W. R. L. (2018). Soil moisture stress as a major driver of carbon cycle uncertainty. *Geophysical Research Letters*, *45*(13), 6495–6503. https://doi.org/10.1029/2018GL078131

van der Tol, C., Rossini, M., Cogliati, S., Verhoef, W., Colombo, R., Rascher,

U., & Mohammed, G. (2016). A model and measurement comparison of diurnal cycles of sun-induced chlorophyll fluorescence of crops. *Remote Sensing of Environment*, *186*, 663–677. https://doi.org/10.1016/j.rse.2016.09.021

van der Tol, C., Verhoef, W., Timmermans, J., Verhoef, A., & Su, Z. (2009). An integrated model of soil-canopy spectral radiances, photosynthesis, fluorescence, temperature and energy balance. *Biogeosciences*, *6*(12), 3109–3129. https://doi.org/10.5194/bg-6-3109-2009

van der Tol, C., Vilfan, N., Dauwe, D., Cendrero-Mateo, M. P., & Yang, P. (2019). The scattering and re-absorption of red and near-infrared chlorophyll fluorescence in the models Fluspect and SCOPE. *Remote Sensing of Environment*, *232*, 111292. https://doi.org/10.1016/j.rse.2019.111292

Verhoef, A., & Egea, G. (2014). Modeling plant transpiration under limited soil water: Comparison of different plant and soil hydraulic parameterizations and preliminary implications for their use in land surface models. *Agricultural and Forest Meteorology*, *191*, 22–32. https://doi.org/10.1016/j.agrformet.2014.02.009

Verhoef, W. (1998). *Theory of radiative transfer models applied in optical remote sensing of vegetation canopies* (Doctral dissertation). Retrieved from Wageningen University and Research Library (https://library.wur.nl/WebQuery/wurpubs/43047). Wageningen: Wageningen Agricultural University.

Verhoef, W., van der Tol, C., & Middleton, E. M. (2018). Hyperspectral radiative transfer modeling to explore the combined retrieval of biophysical parameters and canopy fluorescence from FLEX – Sentinel-3 tandem mission multi-sensor data. *Remote Sensing of Environment*, *204*, 942–963. https://doi.org/10.1016/j.rse.2017.08.006

Verma, M., Schimel, D., Evans, B., Frankenberg, C., Beringer, J., Drewry, D. T., et al. (2017). Effect of environmental conditions on the relationship between solar-induced fluorescence and gross primary productivity at an OzFlux grassland site. Journal of Geophysical Research: *Biogeosciences*, *122*(3), 716–733. https://doi.org/10.1002/2016JG003580

Vermote, E. F., & Vermeulen, A. (1999). *Atmospheric correction algorithm: Spectral reflectances (MOD09) Version 4.0* (NASA contract NAS5-96062). Retrieved from https://modis.gsfc.nasa.gov/data/atbd/atbd_mod08.pdf.

Verrelst, J., Rivera, J. P., van der Tol, C., Magnani, F., Mohammed, G., & Moreno, J. (2015). Global sensitivity analysis of the SCOPE model: What drives simulated canopy-leaving sun-induced fluorescence? *Remote Sensing of Environment*, *166*, 8–21. https://doi.org/10.1016/j.rse.2015.06.002

Wan, Z., Hook, S., Hulley, G. (2015). MYD11A1 MODIS/Aqua Land Surface Temperature/Emissivity Daily L3 Global 1km SIN Grid V006 [Data set]. NASA EOSDIS Land Processes DAAC.

Weiss, M., & Baret, F. (2016). *S2ToolBox Level 2 products: LAI, FAPAR, FCOVER Version 1.1.* Retrieved from https://step.esa.int/docs/extra/ATBD_S2ToolBox_L2B_V1.1.pdf. Avignon: Institut National de la recherche agronomique

Xu, Z., Fan, K., & Wang, H. (2015). Decadal variation of summer precipitation over China and associated atmospheric circulation after the late 1990s. *Journal of Climate*, *28*(10), 4086–4106. https://doi.org/10.1175/JCLI-D-14-00464.1

Yan, K., Park, T., Yan, G., Liu, Z., Yang, B., Chen, C., et al. (2016). Evaluation of MODIS LAI/FPAR product collection 6. Part 2: Validation and intercomparison. *Remote Sensing*, *8*(6), 460. https://doi.org/10.3390/rs8060460

Yan, Y., Yan, R., Chen, J., Xin, X., Eldridge, D. J., Shao, et al. (2018). Grazing modulates soil temperature and moisture in a Eurasian steppe. *Agricultural and Forest Meteorology*, *262*, 157–165. https://doi.org/10.1016/j.agrformet.2018.07.011

Yang, P., Prikaziuk, E., Verhoef, W., & van der Tol, C. (2021). SCOPE 2.0: a model to simulate vegetated land surface fluxes and satellite signals. *Geoscientific Model Development*, *14*(7), 4697–4712. https://doi.org/10.5194/gmd-14-4697-2021

Yang, P., van der Tol, C., Yin, T., & Verhoef, W. (2020). The SPART model: A soil-plant-atmosphere radiative transfer model for satellite measurements in the solar spectrum. *Remote Sensing of Environment*, *247*, 111870. https://doi.org/10.1016/j.rse.2020.111870

Zheng, Y., Shen, R., Wang, Y., Li, X., Liu, S., Liang, S., et al. (2020). Improved estimate of global gross primary production for reproducing its long-Term variation, 1982-2017. *Earth System Science Data*, *12*(4), 2725–2746. https://doi.org/10.5194/essd-12-2725-2020

Zhou, S., Duursma, R. A., Medlyn, B. E., Kelly, J. W. G., & Prentice, I. C. (2013). How should we model plant responses to drought? An analysis of stomatal and non-stomatal responses to water stress. *Agricultural and Forest Meteorology*, *182–183*, 204–214. https://doi.org/10.1016/j.agrformet.2013.05.009